Solutions to data and operator aliasing with the parabolic radon transform

Antoine Guitton[1]

ABSTRACT

Focusing in the radon domain can be affected by data and operator aliasing. Antialiasing conditions can be imposed on the parabolic radon transform (PRT) operator by dip limiting the summation path. These dip limits in time translate into frequency limits in the Fourier domain. Consequently, antialiasing the PRT enables better focusing in the radon domain. If the radon domain is computed *via* inverse theory, a regularization term in either the time or frequency domain can reduce data aliasing effects. The frequency domain regularization has the advantage of being noniterative, but needs to be applied in patches in order to improve focusing.

INTRODUCTION

The parabolic radon transform (PRT) is extensively used to transform the data into a domain where multiples and primaries are separable. This multiple-attenuation method proceeds as follows: the data are sorted in common midpoint (CMP) gathers, flattened with a normal moveout (NMO) correction, and then radon transformed. The multiples are then muted in the radon domain and subtracted from the input data. The final result depends heavily on the mapping of the primaries and multiples in the radon domain.

The limited aperture of the recording geometry and the spatial data sampling might considerably affect the separability of primaries and multiples (Kabir and Marfurt, 1999). This data sampling issue is called data aliasing. It causes many artifacts that dramatically affect focusing in the radon domain (Figure 2).

A second source of problem can stem from aliasing of the radon transform operator. The operator aliasing creates noise in the radon domain by the summation action of the PRT operator on the CMP gather (Abma et al., 1999; Lumley et al., 1994).

In this paper, I present solutions to correct for both operator and data aliasing. We can antialias the operator by imposing dip limitations on the summation path of the PRT. These dip limits translate easily into frequency limits. I also show that when using inverse theory, data-aliasing artifacts can be attenuated by imposing some constraints on the sparseness of the radon domain.

[1]**email:** antoine@sep.stanford.edu

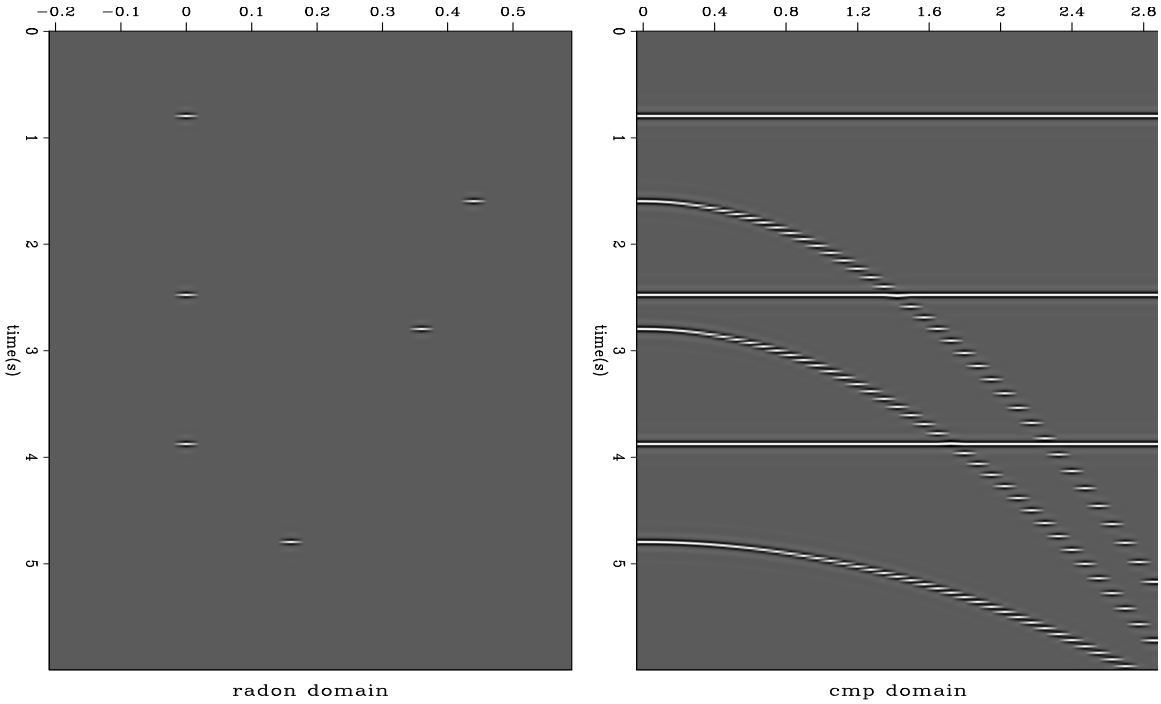

Figure 1: Left: A parabolic radon model ($s.km^{-2}$). Right: Data derived from the left panel using the PRT (offset in km). antoine3-datasynt [ER]

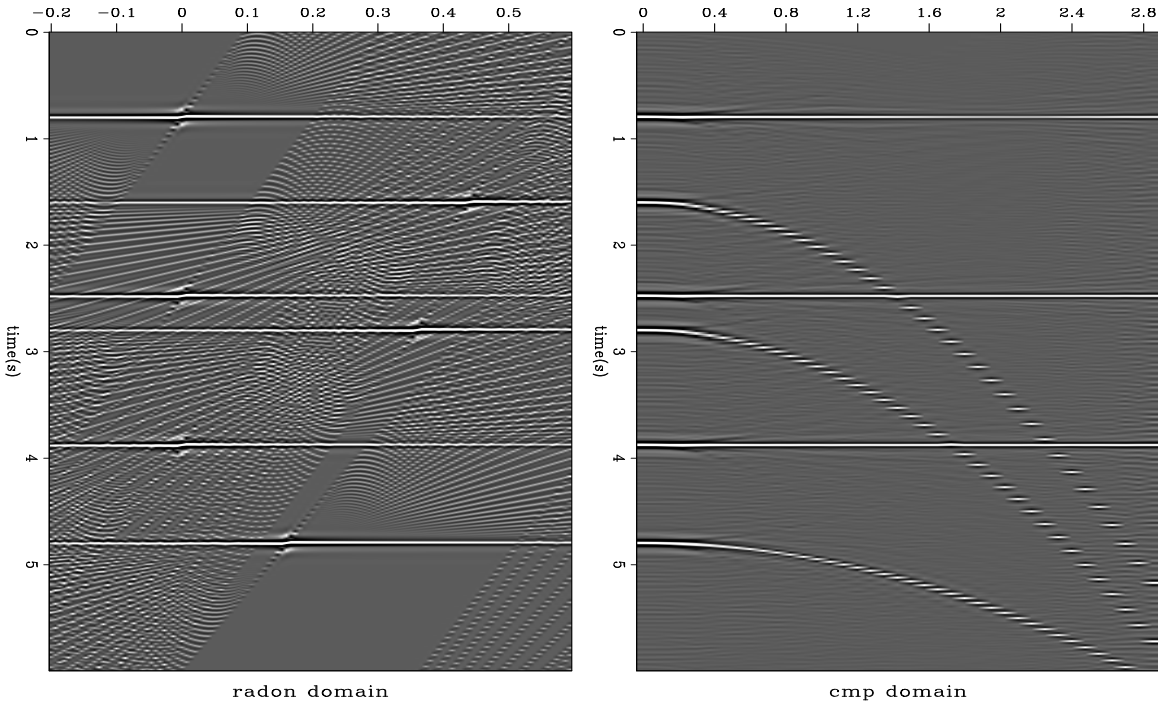

Figure 2: Left: The radon domain obtained by applying the adjoint PRT $\mathbf{L}'$ to the input data shown in Figure 1. The straight lines are caused by the limited aperture of the recording geometry. The other noisy events correspond to data-aliasing noise. Right: Reconstructed data applying the forward operator $\mathbf{L}$ to the left panel. antoine3-radon [ER]

ANTIALIASING THE PARABOLIC RADON TRANSFORM

Aliasing of the operator can be avoided if we limit the dips of the PRT summation path. This dip filtering can be easily implemented in the Fourier domain, which results in a simple frequency limit condition.

Computing the PRT in the Fourier domain

Prior to the dip filtering, however, it is necessary to compute the PRT in the Fourier domain, rather than in the time domain. The equations that follow show a method for computing the PRT in the frequency domain. In the time domain, the equation for a parabola is

$$t(q,x) = \tau + qx^2, \tag{1}$$

where τ is the zero offset time, x the offset, and q the curvature of the parabola. The modeling equation, which superposes on parabolas, from the radon domain to the CMP domain is

$$d(t,x) = \sum_{\tau} \sum_{q} m(\tau,q)\delta(\tau - (t - qx^2)), \tag{2}$$

and the adjoint transform, which sums along parabolas, is

$$m(\tau,q) = \sum_{t} \sum_{x} d(t,x)\delta(t - (\tau + qx^2)). \tag{3}$$

We can easily transform these equations in the Fourier domain as follows:

$$d(\omega,x) = \sum_{q} m(\omega,q)e^{-j\omega qx^2}, \tag{4}$$

$$m(\omega,q) = \sum_{x} d(\omega,x)e^{j\omega qx^2}. \tag{5}$$

With ω constant, equations (4) and (5) describe a simple matrix multiplication with the operator $\mathbf{L}$:

$$\mathbf{L}_{ik} = e^{-j\omega q_k x_i^2}. \tag{6}$$

Hence, we can write equations (4) and (5) in the following more familiar way for each frequency:

$$\mathbf{d} = \mathbf{Lm}, \tag{7}$$

$$\mathbf{m} = \mathbf{L}'\mathbf{d}, \tag{8}$$

where $\mathbf{L}'$ is the adjoint of $\mathbf{L}$. I have computed the radon and offset domains in Figure 2 using equations (7) and (8). The following is a possible algorithm for computing the radon domain:

- Fourier transform the data.

- For each frequency, starting from the lowest to the highest, solve equation (8).
- Inverse Fourier transform **m**.

Because we can compute a *pseudo*-inverse for **L** noniteratively in the Fourier domain (Kostov, 1989), the PRT is generally not computed in the time domain.

Antialiasing conditions for the PRT operator

Antialiasing the operator is equivalent to dip-filtering the operator. The anti-aliasing conditions can be written (Abma et al., 1999) as

$$f_{max} \leq \frac{1}{2\Delta T}, \tag{9}$$

where ΔT is the local slope of the operator between two adjacent traces. For the PRT, we can compute the local slope as follows:

$$\Delta T = \frac{\partial t(q,x)}{\partial x}\Delta x, \tag{10}$$
$$\Delta T = 2qx\Delta x, \tag{11}$$

where Δx is the input trace spacing. The antialiasing condition becomes

$$f_{max} \leq \frac{1}{4qx\Delta x}, \tag{12}$$
$$\omega_{max} \leq \frac{\pi}{2qx\Delta x}. \tag{13}$$

The antialiasing condition in equation (13) is then implemented in the Fourier domain. Figure 3 shows how the antialiasing works in the data space when the adjoint of the PRT ($\mathbf{L}'$) is applied to the model in Figure 1: parabolas broaden with offset as a result of the dip filtering. Thus, the antialiasing operator generates a loss of resolution. We now apply the antialiasing operator to the CMP gather shown in the right-hand panel of Figure 1. The radon domain in Figure 4 (as compared with that in Figure 2) has been cleaned up with a loss of resolution. However, because we apply an antialiasing operator with aliased data, we are left with aliasing noise near $q = 0s/km^2$. This aliasing noise is caused by the aliasing of the non-flat events in the CMP domain. We can mitigate these artifacts by introducing some constraints in the radon domain as a function of the expected aliased dips in the data (Biondi, 1998), but this is not considered here. Nonetheless, we see that the use of an antialiasing operator with aliased data is worthwhile. In addition, cleaning up the aliasing artifacts for a high q is particularly interesting when multiples are present in the data. Indeed, multiples, often aliased in the CMP domain, map in regions of high q where the antialiasing operator is the most efficient.

In the next section, I investigate the effects of the antialiasing operator when the radon domain is derived with a least-squares approach.

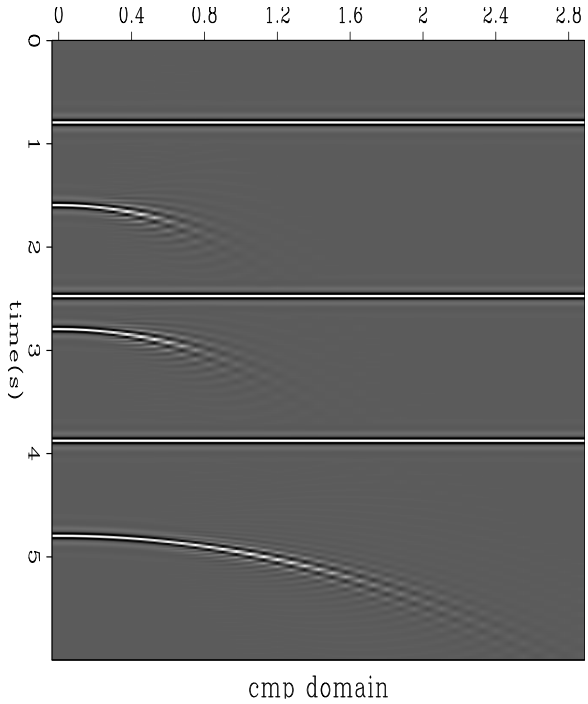

Figure 3: Effects of antialiasing in the data space. The parabolas broaden with offset as a result of the low-pass filtering for large qs. antoine3-data_spikena [ER]

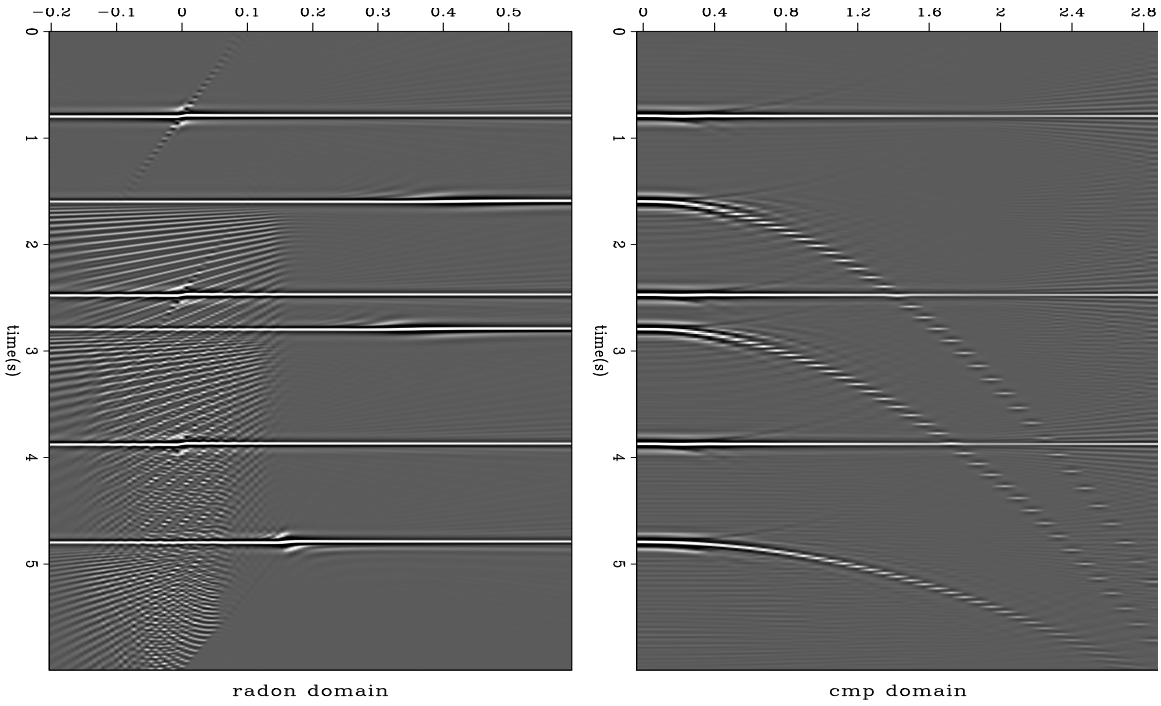

Figure 4: Left: The parabolic radon domain after use of the antialising condition. The aliasing artifacts have decreased. Right: The reconstructed data after the forward operator is applied to the left panel. antoine3-noal [ER]

Operator antialiasing and least-squares inversion

The PRT in the Fourier domain allows us to derive a least-squares estimate of the data in the radon domain. Equations (7) and (8) suggest the use of inversion to recover the original amplitude in the data. In computing the pseudo-inverse of the matrix **L**, two cases need to be distinguished.

The under-determined case: The least-squares inverse of **m** for each frequency is

$$\hat{\mathbf{m}}_{\mathbf{under}} = \mathbf{L}'(\mathbf{L}\mathbf{L}' + \epsilon\mathbf{I})^{-1}\mathbf{d}, \tag{14}$$

where $\hat{\mathbf{m}}$ is the estimate of the model, $\mathbf{L}\mathbf{L}' + \epsilon\mathbf{I}$ a matrix $nx \times nx$ to invert, and $\epsilon = \sigma_d^2/\sigma_m^2$.

The over-determined case: The least-squares inverse for **m** for each frequency is

$$\hat{\mathbf{m}}_{\mathbf{over}} = (\mathbf{L}'\mathbf{L} + \epsilon\mathbf{I})^{-1}\mathbf{L}'\mathbf{d}, \tag{15}$$

where $\mathbf{L}'\mathbf{L}+\epsilon\mathbf{I}$ is a $nq \times nq$ matrix to invert with a Toeplitz structure (Kostov, 1989; Darche, 1990).

An interesting problem occurs when the conditioning of the matrix quickly deteriorates as frequencies increase. This effect is partly caused by the frequency truncation of the operator. A solution to this problem is to increase ϵ, which appears in equations (14) and (15), with the frequency. To do so, I set

$$\epsilon_\omega = \log(n_w + 1) * \beta, \tag{16}$$

where n_w is the index of the computing frequency and β a constant to set *apriori*. This choice of ϵ_ω allows us to increase the regularization with the frequency but not too much. Indeed a too strong regularization would affect the amplitude recovery of the data.

The size of the matrix to invert makes possible the use of direct inversion as opposed to iterative processes. Figure 5 shows the result of inversion using the aliased operator. The aliasing artifacts are still strong, but some energy has focused, decreasing the width of the horizontal events caused by near-offset aperture effects. The resulting data, which appear in the right panel of Figure 5, are almost perfectly recovered. The residual in the left panel of Figure 7 demonstrates that the data fitting is nearly perfect.

Now, using the antialiasing conditions on the operator, we obtain the data in Figure 6: events are better focused in the radon domain and most of data aliasing artifacts have disappeared. We observe a loss of resolution for the non-flat events caused by the antialiasing conditions. The aliasing of the input data produces the remaining noisy events in the radon domain. Again, the data in the right panel of Figure 6 are almost completely recovered, and the residual in the right panel of Figure 7 is very small.

This result proves that the antialiasing PRT can be inverted as long as ϵ is provided. It also proves that the use of antialiasing conditions on the operator helps to mitigate data aliasing artifacts. However, as Figure 6 indicates, data aliasing effects can't be totally removed. The next section shows that sparseness conditions in the radon domain can destroy data aliasing artifacts.

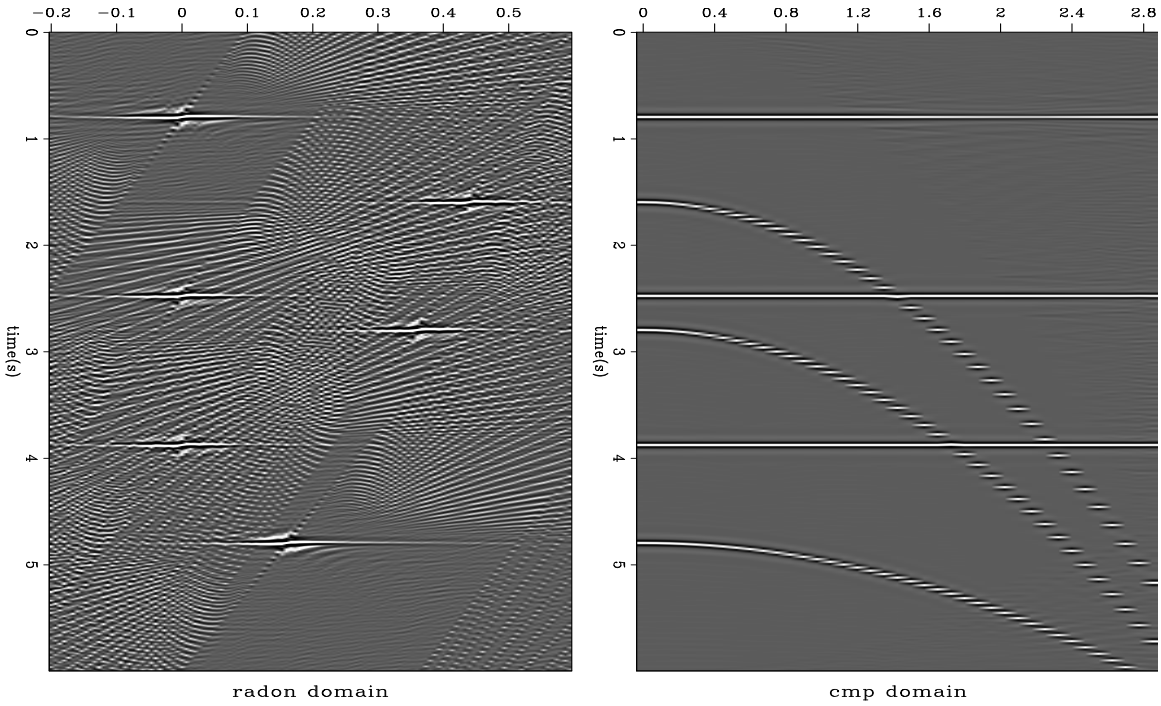

Figure 5: Left: The parabolic radon domain after least-squares inversion. The events of interest are more focused, but the aliasing artifacts remain. Right: The reconstructed data; the result is nearly perfect. antoine3-inval [ER]

REMOVING DATA ALIASING ARTIFACTS

Inverse theory offers an attractive framework for designing solvers that will enforce sparseness in the radon domain (Sacchi and Ulrych, 1995; Nichols, 1994). These solvers impose focusing in the model space by adding a regularization term in the objective function, which then penalizes small values. This section presents two methods that address data aliasing. One method is generally used in the time domain, and the other is specifically designed to work in the frequency domain (Herrmann et al., 2000). For data examples of the time domain method, the reader can refer to Guitton (2000) and Nichols (1994). Synthetic and real data examples of the frequency domain method follow my description of it.

The time domain approach

The sparse solver in the time domain employs a regularization term that enforces spikyness in the model space (Nichols, 1994). This approach is well-suited for time-domain processing and makes use of iterative solvers as opposed to direct inversion as described in equations (14) and (15). For instance, by choosing an approximation of the ℓ^1 norm for the model space regularization, we can focus the energy of the model vector $\mathbf{m}$ into its main components. Ulrych et al. (2000) advocate a regularization by the Cauchy-Gauss model. In any case, the

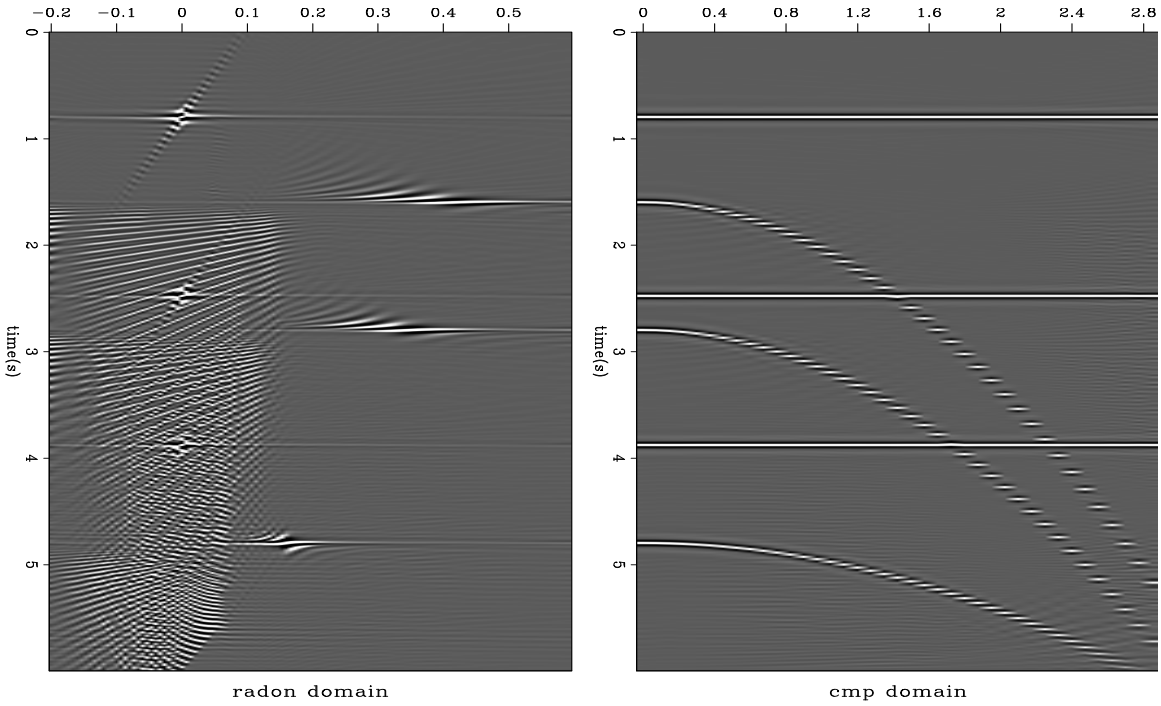

Figure 6: Left: The parabolic radon domain after inversion of the antialiasing operator. The events are more focused and the aliasing artifacts have been weakened. We see a loss of resolution caused by the antialiasing conditions. The aliasing of the input data produces the remaining noisy events. Right: The reconstructed data. antoine3-invna [ER]

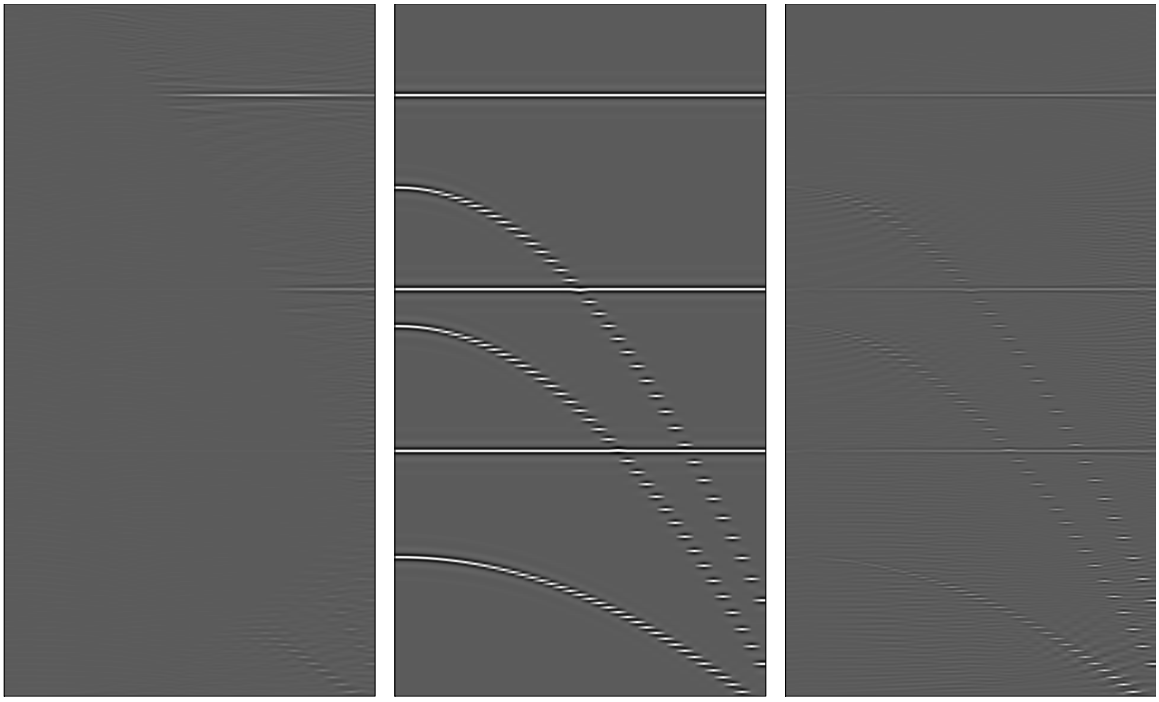

Figure 7: Left: Residual for the aliased operator with least-squares inversion. Middle: Input data. Right: Residual for the antialiasing operator with least-squares inversion. antoine3-comp [ER]

objective function to minimize becomes

$$f(\mathbf{m}) = \|\mathbf{Lm} - \mathbf{d}\|^2 + \epsilon |\mathbf{m}|_{sparse}, \tag{17}$$

where $\|.\|$ is the ℓ^2 norm and where $|.|_{sparse}$ induces a sparse model. Iteratively reweighted least-squares algorithms with the proper weighting function produce an artifact-free model space (Bube and Langan, 1997). A more ambitious Huber norm can be used as well (Guitton and Symes, 1999) for the ℓ^1 case.

The frequency domain approach

In contrast, the method developed by Herrmann et al. (2000) computes an approximation of the model covariance matrix in the Fourier domain. The main idea is to use the result of the inversion, as shown in equations (14) and (15), at one frequency as a weight for the next frequency. Consequently, this method takes advantage of the fact that the data are not aliased at low frequencies. Hence, the information from the lowest frequencies to the highest is transmitted and used to improve the focusing in the model space. I call this method the steering-weighting matrices method. It has the advantage of working noniteratively.

Taking this approach, starting from $\omega = \omega_{min}$ up to $\omega = \omega_{max}$, we begin with the two fitting

goals for each frequency

$$\mathbf{0} \approx \mathbf{L}_\omega \mathbf{m}_\omega - \mathbf{d}_\omega, \tag{18}$$
$$\mathbf{0} \approx \epsilon_\omega^{1/2} \mathbf{W}_\omega^{-1/2} \mathbf{m}_\omega, \tag{19}$$

where the diagonal matrix $\mathbf{W}$ has components

$$W_\omega^{ii} = |\hat{m}_{\omega-1}^i|, \tag{20}$$

with $\mathbf{W}_{\omega_{min}} = \mathbf{I}$. The division in equation (19) can be avoided if we use $\mathbf{W}_{\omega-1}^{-1/2}$ as a preconditioning operator (Fomel, 1997). Then, omitting the ω, we obtain

$$\mathbf{0} \approx \mathbf{L}\mathbf{W}^{1/2}\mathbf{x} - \mathbf{d}, \tag{21}$$
$$\mathbf{0} \approx \epsilon^{1/2}\mathbf{x}, \tag{22}$$

with $\mathbf{x} = \mathbf{W}^{-1/2}\mathbf{m}$. The estimate of the model can be written as follows:

$$\hat{\mathbf{m}} = \mathbf{W}\mathbf{L}'(\mathbf{L}\mathbf{W}\mathbf{L}' + \epsilon\mathbf{I})^{-1}\mathbf{d}, \tag{23}$$

or equivalently as

$$\hat{\mathbf{m}} = (\mathbf{L}'\mathbf{L} + \epsilon\mathbf{W}^{-1})^{-1}\mathbf{L}'\mathbf{d}. \tag{24}$$

Equation (23), used in the under-determined case, is clearly easier to compute because we do not have to calculate $\mathbf{W}^{-1}$. Since in practice we often have to deal with more unknowns than data points, I use equation (23) in the following examples.

Results with the frequency domain approach

I implemented this method with synthetic and real data. The synthetic case perfectly attenuates the aliasing artifacts. The real data case is not as convincing however, because we have a dense information in the data space to interpret with few parabolas in the model space.

The result with synthetic data is striking (Figure 8): all the artifacts have disappeared, leaving a clean model space. The data are almost entirely recovered. Figure 9 displays the diagonal elements of the matrix $\mathbf{W}$ at each frequency. We can see that from the lowest to the highest frequencies, the diagonal elements focus at four different locations corresponding to the four parabolic curvatures present in the input data. The cut-off at 70 Hz which corresponds to the highest frequency component present in the data, is used to calculate the model space.

With real data, however, the results suggest strategies to better focus the radon domain. Figure 10 shows the inversion of one CMP gather in the parabolic radon domain when no attempt were made to focus the model space components, that is, no weight in equation (23). The residual is displayed in the right panel of Figure 12. Although the inversion produces a satisfactory fitting of the input data, some aliasing artifacts appear in the radon domain. Figure 11 displays the result of the inversion using the steering-weighting matrices. It shows that fewer artifacts appear in the radon domain. A comparison of the residual with and without

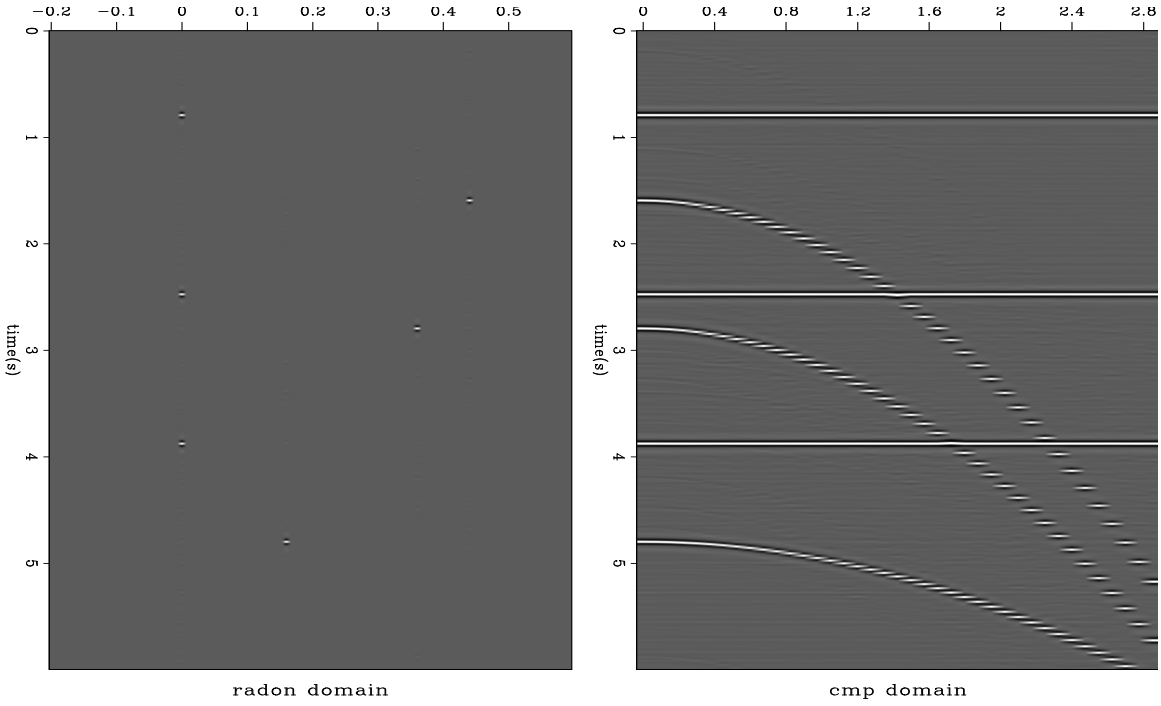

Figure 8: Left: Model space using the steering matrices. Right: Data reconstructed from the left panel. The aliasing artifacts are gone, and the focusing in the model space is perfect. antoine3-spikeal [ER]

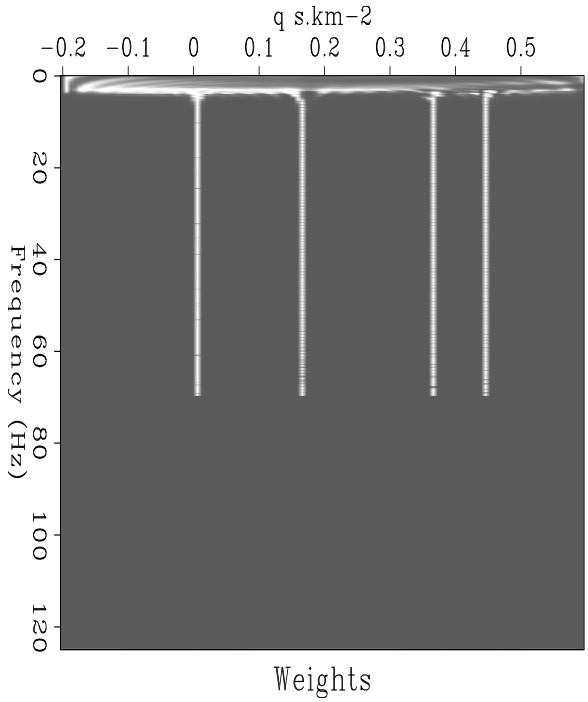

Figure 9: Diagonal elements of the weighting matrix **W** at each frequency. The four stripes correspond to the location of the four curvatures in the radon domain. The cut-off at 70 Hz corresponds to the highest frequency present in the data. antoine3-weight [ER]

weight , shown in Figure 12, demonstrates that the data fitting is satisfactory for both cases. It turns out that the crucial parameter is ϵ_ω. I don't have any guideline for choosing it but trial and error. The efficiency of the steering-weighting matrices method is based on the number of parabolic events present in the data. The best results are achieved when few events have to be focused in a large radon domain. However, since for real data cases this requirement may be difficult to meet, I anticipate no or few improvements if we use this method. One solution may be simply to apply it to different patches as suggested by Herrmann et al. (2000).

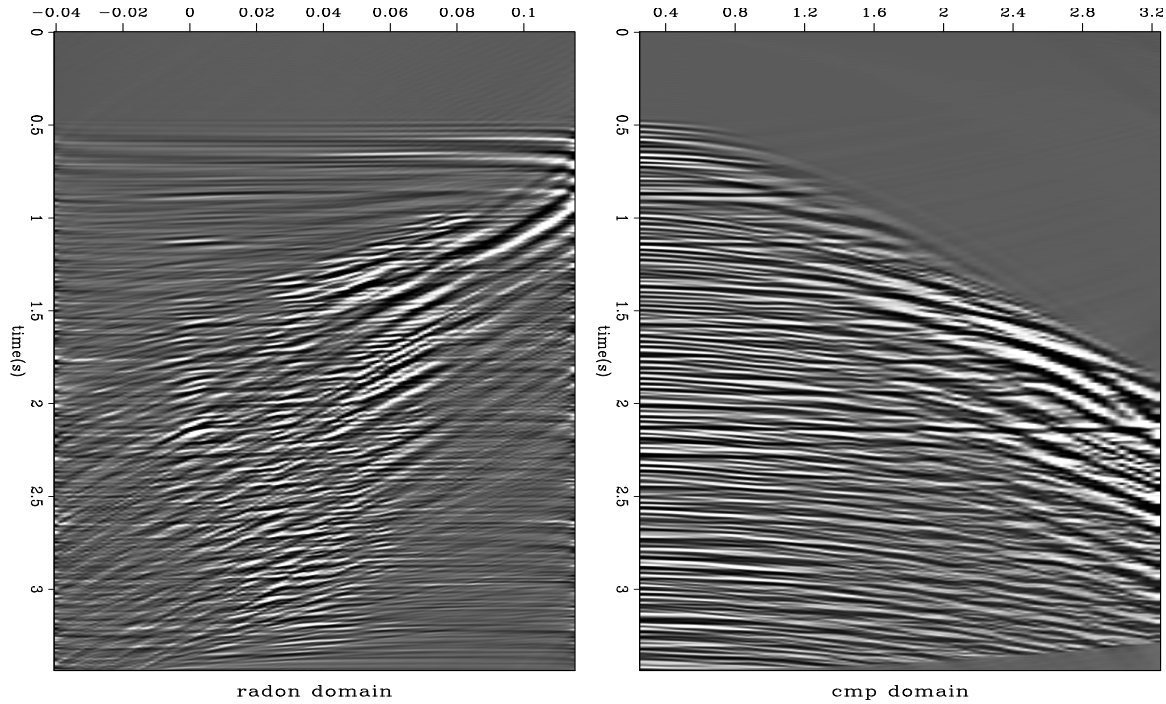

Figure 10: Left: A radon domain obtained using inversion without steering matrices. Right: The reconstructed data. antoine3-nmo2 [ER]

CONCLUSION

The inversion of the PRT can be done quickly in the Fourier domain using a least-squares inverse. Employing an antialiasing operator helps focus more precisely in the radon domain. I demonstrated that data aliasing effects can be eliminated using a sparse solver in the time or frequency domain. The frequency domain solution, however, may need to be applied in patches.

REFERENCES

Abma, R., Sun, J., and Bernitsas, N., 1999, Antialiasing methods in Kirchhoff migration: Geophysics, **64**, no. 6, 1783–1792.

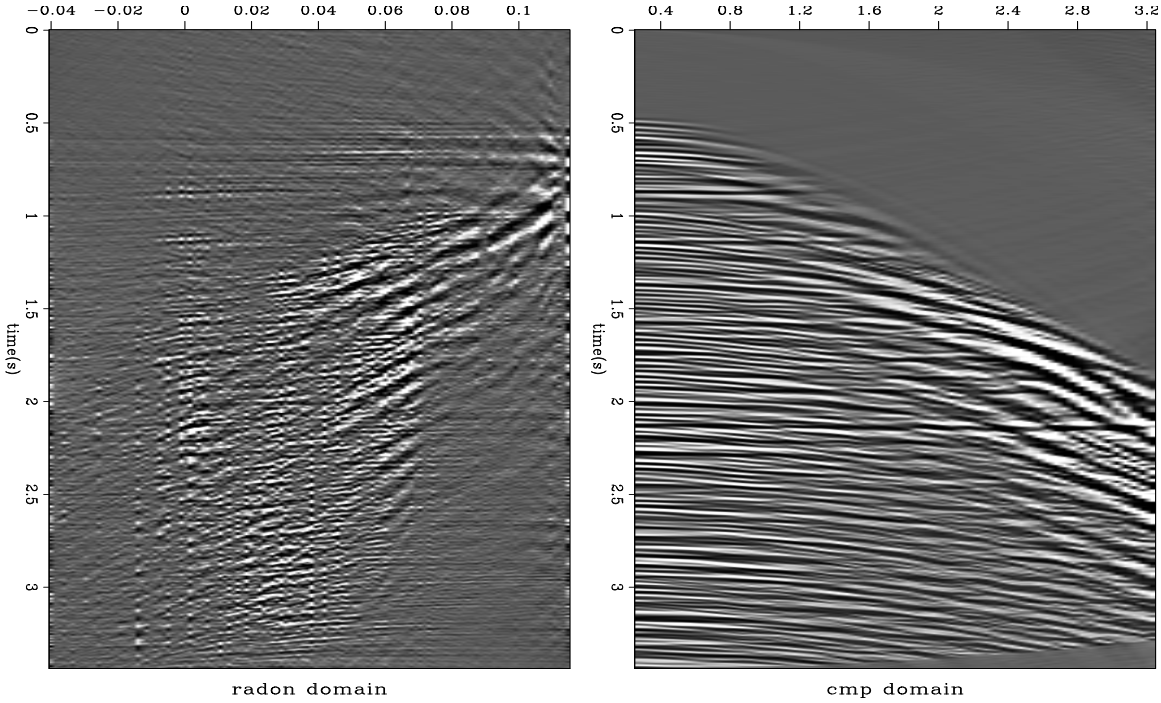

Figure 11: Left: A radon domain obtained using inversion with steering matrices. Right: The reconstructed data. antoine3-nmo1 [ER]

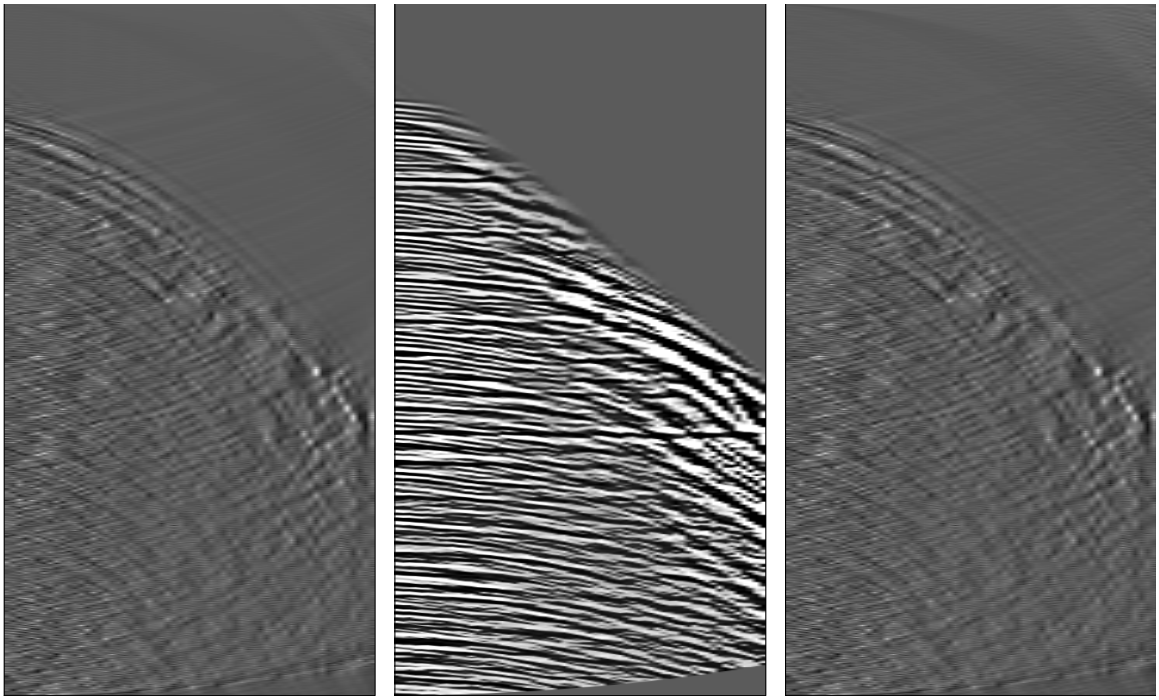

Figure 12: Left: Residual of the inversion in Figure 10 using the steering matrices. Middle: Input data. Right: Residual of the inversion in Figure 11 without the steering matrices. antoine3-comp2 [ER]

Biondi, B., 1998, Kirchhoff imaging beyond aliasing: SEP–**97**, 13–34.

Bube, K. P., and Langan, R. T., 1997, Hybrid lambda1/lambda2 minimization with applications to tomography: Geophysics, **62**, no. 04, 1183–1195.

Darche, G., 1990, Fast parabolic transforms: SEP–**65**, 99–112.

Fomel, S., 1997, On model-space and data-space regularization: A tutorial: SEP–**94**, 141–164.

Guitton, A., and Symes, W., 1999, Robust and stable velocity analysis using the Huber function: 69th Annual Internat. Mtg., Soc. Expl. Geophys., Expanded Abstracts, 1166–1169.

Guitton, A., 2000, Prestack multiple attenuation using the hyperbolic Radon transform: SEP–**103**, 181–201.

Herrmann, P., Mojesky, T., Magesan, M., and Hugonnet, P., 2000, De-aliased high-resolution Radon transform: 70th Annual International Meeting, Society Of Exploration Geophysicists, Annual Meeting Abstracts, 1953–1956.

Kabir, M. M. N., and Marfurt, K. J., 1999, Toward true amplitude multiple removal: The Leading Edge, **18**, no. 1, 66–73.

Kostov, C., 1989, Finite-aperture slant stack transforms: SEP–**61**, 261–280.

Lumley, D. E., Claerbout, J. F., and Bevc, D., 1994, Anti-aliased Kirchhoff 3-D migration: 64th Annual Internat. Mtg., Soc. Expl. Geophys., Expanded Abstracts, 1282–1285.

Nichols, D., 1994, Velocity-stack inversion using $\mathbf{L_p}$ norms: SEP–**82**, 1–16.

Sacchi, M. D., and Ulrych, T. J., 1995, High-resolution velocity gathers and offset space reconstruction: Geophysics, **60**, no. 04, 1169–1177.

Ulrych, T. J., Sacchi, M. D., and Woodbury, A., 2000, A Bayes tour of inversion: A tutorial: Geophysics, **66**, no. 1, 55–69.